

Post-merger evolution of carbon-oxygen + helium white dwarf binaries and the origin of R Coronae Borealis and extreme helium stars

Xianfei Zhang^{1*}, C. Simon Jeffery^{1,2†}, Xuefei Chen^{3,4}, and Zhanwen Han^{3,4}

¹*Armagh Observatory, College Hill, Armagh BT61 9DG, UK*

²*School of Physics, Trinity College Dublin, Dublin 2, Ireland*

³*Yunnan Observatories, Chinese Academy of Sciences, Kunming 650011, China*

⁴*Key Laboratory for the Structure and Evolution of Celestial Objects, Chinese Academy of Sciences, Kunming, 650011, PR China*

Accepted . Received ; in original form

ABSTRACT

Orbital decay by gravitational-wave radiation will cause some close-binary white dwarfs (WDs) to merge within a Hubble time. The results from previous hydrodynamical WD-merger simulations have been used to guide calculations of the post-merger evolution of carbon-oxygen + helium (CO+He) WD binaries. Our models include the formation of a hot corona in addition to a Keplerian disk. We introduce a “destroyed-disk” model to simulate the effect of direct disk ingestion into the expanding envelope. These calculations indicate significant lifetimes in the domain of the rare R Coronae Borealis (RCB) stars, before a fast evolution through the domain of the hotter extreme helium (EHe) stars. Surface chemistries of the resulting giants are in partial agreement with the observed abundances of RCB and EHe stars. The production of ^3He , ^{18}O and ^{19}F are discussed. Evolutionary timescales combined with binary white-dwarf merger rates from binary-star population synthesis are consistent with present-day numbers of RCBs and EHes, provided that the majority come from relatively recent ($< 2\text{Gyr}$) star formation. However, most RCBs should be produced by CO-WD + *low-mass* He-WD mergers, with the He-WD having a mass in the range $0.20 - 0.35 M_{\odot}$. Whilst, previously, a high He-WD mass ($\geq 0.40 M_{\odot}$) was required to match the carbon-rich abundances of RCB stars, the “destroyed-disk” model yields a high-carbon product with He-WD mass $\geq 0.30 M_{\odot}$, in better agreement with population synthesis results.

Key words: stars: peculiar (helium), stars: evolution, stars: white dwarfs, stars: abundances, binaries: close

1 INTRODUCTION

R Coronae Borealis (RCrB or RCB) stars are carbon-rich, hydrogen-poor supergiants (Clayton 1996). They range in effective temperature (T_{eff}) from 4 000 to 8 000 K. The surface gravities range from $\log g = 0.5$ to 1.5 . Due to the ejection and condensation of carbon-rich dust clouds (soot), RCBs show large visible brightness variations. The RCB population in the Large Magellanic Cloud (LMC) provides estimates of absolute magnitudes which range from $M_V \sim 2.5$ to ~ 5 and corresponding luminosities $\log(L/L_{\odot})$ of 4.0 to 3.2 (Alcock et al. 2001). At present, about 68 RCBs are known in the Galaxy, 25 in the Magellanic Clouds, and 4 in M31

(Clayton 1996; Zaniewski et al. 2005; Tisserand et al. 2008; Clayton 2012; Tang et al. 2013).

The surface compositions of RCB stars are extremely helium-rich (mass fraction 0.98). Besides extreme hydrogen deficiency, RCB stars are enriched in N, Al, Na, Si, S, Ni, several s-process elements, and sometimes O (Lambert 1986; Asplund et al. 2000). The isotopic carbon ratio, $^{12}\text{C}/^{13}\text{C}$, is very large (> 500) in most RCB stars (Clayton et al. 2007). In most RCB stars where oxygen isotopic ratios can be measured, ^{18}O is enhanced relative to ^{16}O by factors of $100\sim 1000$ compared to standard Galactic values. In addition, some RCB stars are enhanced in lithium (Asplund et al. 2000).

Extreme Helium stars (EHe) are early-type supergiants with spectral types A and B and atmospheres almost void of hydrogen, but highly enriched in carbon (Jeffery et al. 2011). In many respects, their surface composition resem-

* E-mail: xiz@arm.ac.uk

† E-mail: csj@arm.ac.uk

bles that of the RCB stars, although isotopic ratios and the abundances of some interesting elements cannot be measured. Because of these similarities, a strong link between the cool RCB and the hot EHe stars has been postulated.

By considering these characteristics, two principle evolution channels have been established. A small fraction may be produced following a late thermal pulse in a post-asymptotic giant-branch star on the white dwarf cooling sequence (Iben & Renzini 1984; Clayton et al. 2011). The majority are more likely to have been produced following the merger of a carbon-oxygen white dwarf with a helium white dwarf (Webbink 1984; Saio & Jeffery 2002; Jeffery et al. 2011; Longland et al. 2011; Staff et al. 2012; Menon et al. 2013; Dan et al. 2014). Less than 1% of RCB stars may come from a high-mass double helium white dwarf merger (Zhang & Jeffery 2012a).

Using a simple nuclear reaction model, Clayton et al. (2007) indicated that in a CO+He WD merger, it is partial $^{14}\text{N}+^4\text{He}$ burning at just the right temperature and duration that is the likely generator of excess ^{18}O (or a small $^{16}\text{O}/^{18}\text{O}$ ratio). In addition, the high values of $^{12}\text{C}/^{13}\text{C}$ observed in RCB stars are probably produced by 3α burning at the same time. Using complete nucleosynthesis models for asymptotic giant branch (AGB) stars as indicative of the composition of the CO white dwarf progenitor, Jeffery et al. (2011) examined the elements produced during a CO+He WD merger; the results supported such a merger as a possible progenitor of RCB stars. Smoothed-particle hydrodynamics (SPH) simulations have sought to probe the physics of the merger itself (Yoon et al. 2007; Lorén-Aguilar et al. 2009; Longland et al. 2012; Zhu et al. 2013). Those SPH simulations indicated that before the slow or ‘cool’ disk-accretion phase (Saio & Jeffery 2002), there would have been a fast or ‘hot’ accretion phase. This fast phase may last between a few minutes (in unsynchronized systems) and a few hours (Raskin et al. 2012; Dan et al. 2011), during which approximately half the accreted mass would form a hot corona around the more massive star. Since none of the SPH calculations address the long-term post-merger evolution, and the Saio & Jeffery (2002) models did not incorporate a hot coronal phase, the picture of the post-merger evolution of a CO+He WD binary remains incomplete.

In this paper, we construct one-dimensional stellar evolution models for a number of *dynamical* CO+He WD mergers guided by the results of recent SPH calculations. These models are evolved through the RCB domain. The surface chemistries produced by the mergers and their subsequent evolution are compared with observations of RCB stars and related objects.

2 CARBON-OXYGEN + HELIUM WHITE DWARF MERGERS

There are two key requirements for a close binary white dwarf to merge and form a single star. The first is gravitational radiation whereby a close binary star system loses orbital angular momentum J_{orb} and causes the binary separation a to decay until the larger star fills its Roche lobe. The rate of loss of orbital angular momentum (Landau & Lifshitz 1962) is expressed as

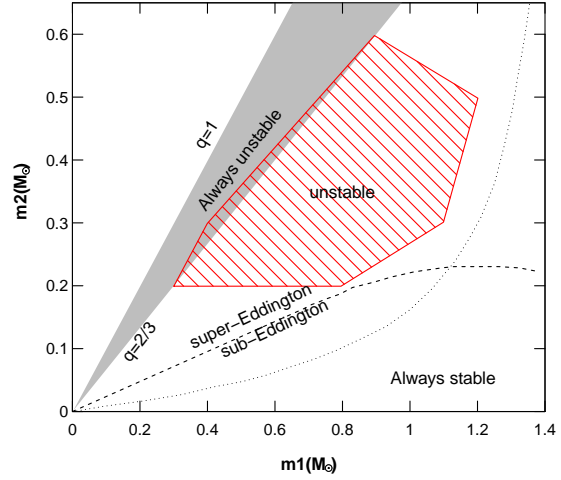


Figure 1. Mass transfer in double WD binaries. Binaries below the dotted line will transfer mass by stable Roche-Lobe overflow (RLOF) and evolve into stable disk-accreting AM CVn binaries. The dashed line separates sub- and super-Eddington accretion systems. Mass transfer in the grey region will be unstable and will lead to dynamical mergers. The area between the solid ($q = 2/3$) and dashed lines corresponds to either stable or unstable mass transfer depending on the spin-orbit coupling. The hatched region marks the area studied by Dan et al. (2011).

$$\frac{\dot{J}_{\text{orb}}}{J_{\text{orb}}} = -8.3 \times 10^{-10} \times \left(\frac{m_1}{M_{\odot}} \right) \left(\frac{m_2}{M_{\odot}} \right) \left(\frac{m_1 + m_2}{M_{\odot}} \right) \left(\frac{a}{R_{\odot}} \right)^{-4} \text{yr}^{-1},$$

where m_1 and m_2 are the masses of stars in the binary.

The second requirement is the mass ratio q . If, at the point where the larger (less massive) white dwarf fills its Roche lobe and starts to lose mass,

$$q \equiv m_2/m_1 \geq q_{\text{crit}} \equiv \frac{5}{6} + \frac{\zeta(m_2)}{2},$$

where $\zeta(m_2) \equiv d \ln r / d \ln m$ is obtained from the white-dwarf mass-radius relation, its radius will increase more quickly than the separation will increase due to the transfer of angular momentum, i.e. the synchronisation timescale of spin-orbit coupling, $\tau_s \rightarrow 0$. This leads to unstable (run-away) mass transfer on a dynamical timescale (a few seconds), corresponding to the grey zone in Fig. 1. However, Nelemans et al. (2001) point out that there is a much more stringent condition under which no angular momentum is transferred from accretor to donor, i.e. the synchronisation timescale of spin-orbit coupling, $\tau_s \rightarrow \infty$. Under this condition, q_{crit} could decrease to $1/5$, as shown by the dotted line in Fig. 1. If $q \leq q_{\text{crit}}$, stable mass transfer will occur, possibly leading to the formation of an AM CVn binary - an ultrashort binary system containing two helium white dwarfs. Thus, white dwarf binaries with mass ratios in the range $2/3 < q < 1$ will merge dynamically. In the region below the dotted line, mass transfer is always stable. The

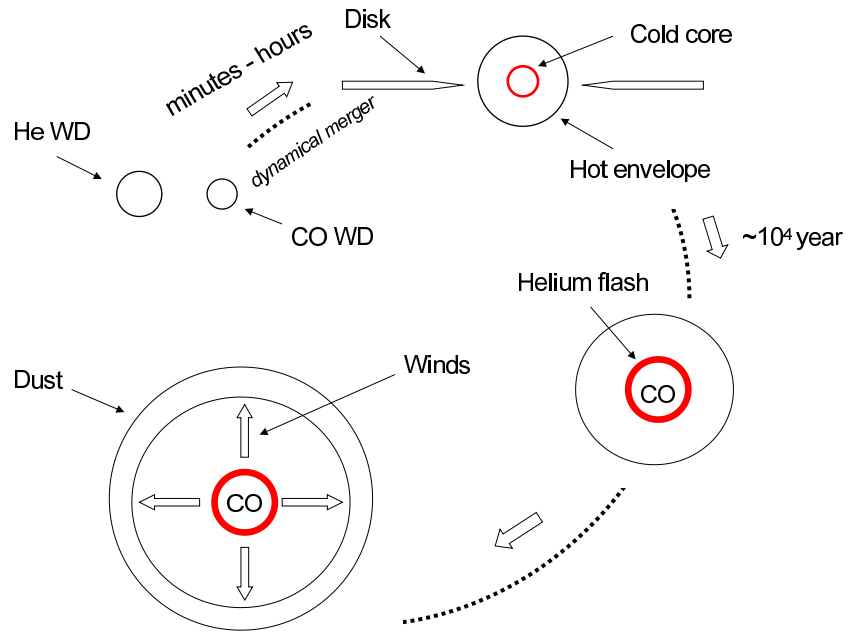


Figure 2. Schematic of possible steps in a carbon-oxygen + helium white dwarf merger leading to the formation an RCB star.

region between both zones corresponds to either stable or unstable mass transfer depending on the spin-orbit coupling (Marsh et al. 2004). The dashed line in Fig. 1 separates sub- and super-Eddington accretion. Under strong coupling, numerical simulations (Motl et al. 2007) indicate that $q < 2/3$ results in stable mass transfer, $2/3 < q < 0.9$ leads to merger and tidal disruption of the donor, and for $q > 0.9$, the donor plunges into the accretor. Under weak coupling, the simulation of Dan et al. (2011) shows that some low mass-ratio binaries will be unstable and experience super-Eddington accretion (hatched zone of Fig. 1).

Hydrodynamical simulations of the merger of two low-mass white dwarfs suggest a number of phases occur. Following the complete tidal disruption of the lower mass component (secondary, m_2), its material may be redistributed around the more massive component (primary, m_1) in (a) a cold Keplerian debris disk and (b) a hot spherical corona. A disk allows cold mass to migrate towards its centre, from where it can be accreted slowly onto the primary surface, while angular momentum is dissipated towards the disk cir-

cumference (Lynden-Bell & Pringle 1974). Fig. 2 shows a simplified sequence of events during a CO + He WD merger as suggested by hydrodynamical simulations. First, the He white dwarf is disrupted by the CO white dwarf in a few minutes, and forms a cold Keplerian debris disk and a hot spherical corona. Then, mass accretion starts from the disk to the star; this process may take around 10^4 years. Once the accreted envelope is massive enough, stable helium-shell burning is ignited and the star becomes a cool giant. At large radius and low T_{eff} , a stellar wind, pulsation and soot formation will give the star the characteristics of an R CrB variable. In addition, a number of RCB stars show nebular emission and extended low-temperature dust shells (Clayton 1996). These are not seen in EHe stars. It is not yet clear whether this circumstellar material is related to the merger process or not.

Table 1. Summary of the ‘corona+disk’ accretion models described in §3.2, showing for each experiment the mass of the carbon-oxygen white dwarf m_{CO} , the helium white dwarf m_{He} , the corona mass m_{corona} , the disk mass m_{disk} , and the final mass of the merger product m_{final} , all in solar units.

Model	m_{CO}	m_{He}	m_{corona}	m_{disk}	m_{final}
1	0.50	0.40	0.23	0.17	0.90
2	0.50	0.45	0.31	0.14	0.95
3	0.55	0.35	0.15	0.20	0.90
4	0.55	0.40	0.20	0.20	0.95
5	0.55	0.45	0.25	0.20	1.00
6	0.60	0.30	0.10	0.20	0.90
7	0.60	0.35	0.12	0.23	0.95
8	0.60	0.40	0.16	0.24	1.00

3 MODELS

3.1 Numerical simulations

Numerical simulations of stellar evolution have been carried out using the stellar evolution code “Modules for Experiments in Stellar Astrophysics” (MESA) version 4028 (Paxton et al. 2011). Carbon-oxygen white-dwarf models were generated by evolving a $3M_{\odot}$ main-sequence star and removing the envelope when this reached the required mass (see Zhang & Jeffery (2012b) for details). The post-merger evolution was modeled by considering fast accretion at $10^4 M_{\odot}\text{yr}^{-1}$, representing the formation of a hot corona, followed by slow accretion at $10^{-5} M_{\odot}\text{yr}^{-1}$, representing accretion from a Keplerian disk. After the accretion process, we employ a Böcker-type stellar wind of the form:

$$P_0 < 100\text{d} :$$

$$\dot{M} = \dot{M}_{\text{R}} \equiv 4 \times 10^{-13} \eta_{\text{R}} \frac{LR}{M} \frac{M_{\odot}}{L_{\odot} R_{\odot}} M_{\odot}\text{yr}^{-1}$$

and

$$P_0 > 100\text{d} :$$

$$\dot{M} = 4.83 \times 10^{-9} \left(\frac{M_{\text{ZAMS}}}{M_{\odot}} \right)^{-2.1} \left(\frac{L}{L_{\odot}} \right)^{2.7} \dot{M}_{\text{R}} M_{\odot}\text{yr}^{-1}$$

where the fundamental-mode pulsation period P_0 is approximated by

$$P_0 = 0.012 \left(\frac{R}{R_{\odot}} \right)^{1.86} \left(\frac{M}{M_{\odot}} \right)^{-0.73} \text{d}$$

(Böcker 1995), and where we adopt two alternative values for the Reimers’ coefficient $\eta_{\text{R}} = 0.02$ and 0.1 . The value normally adopted for Galactic giants is 0.1 . Adopting the smaller value of 0.02 makes some sense for C-rich giants, but the effect of hydrogen deficiency on the mass-loss efficiency is not at all known. The value 0.02 is in agreement with the luminosity and mass loss rates of some lithium and carbon-rich AGB stars in the Magellanic Clouds given by Ventura et al. (2000, 2013), and used for the modelling the thermally-pulsing AGB phase (Lau et al. 2008). The composition of the accreted material is assumed to be $Y = 0.98, Z = 0.02$, where the detailed metal abundance distribution is obtained from the average abundance of the He WD model. We set the ratio of mixing length to local pressure scale height, $\alpha = l/H_{\text{p}} = 2.0$. The opacity tables for various metallicities are those compiled by Grevesse & Sauval (1998) and

Ferguson et al. (2005). The default model atmosphere is an Eddington grey photosphere. The model resolution is determined by an adaptive grid in mass and an adaptive timestep. Nuclear burning is computed and applied explicitly for every timestep in the evolution calculation. Rotation is not treated in the version of MESA used. The evolution calculations do not yet follow the entire evolution through the EHe phase owing to numerical instabilities associated with the very narrow helium-burning shell.

3.2 Hot corona and disk masses: $m_{\text{corona}}, m_{\text{disk}}$

As Zhang & Jeffery (2012a,b) discussed, the final surface composition of the merger depends strongly on the relative mass fractions in the hot corona and the disk. Zhu et al. (2013) studied a detailed parameter space for double carbon-oxygen white dwarf mergers with an SPH simulation, restricted to the systems without tidal locking. They give a formula for the masses of the accretor (m_1) and core-corona ($m_{\text{ce}} = m_1 + m_{\text{corona}}$) as:

$$\frac{m_{\text{ce}}}{m_1} = 1 + 0.81q_{\rho} \pm 0.03,$$

where q_{ρ} is the central density ratio of the donor ($m_2 = m_{\text{disk}} + m_{\text{corona}}$) and accretor (m_1), $q_{\rho} \equiv \rho_{c,2}/\rho_{c,1}$. In the mass range of 0.4 to $1.0 M_{\odot}$, the central density ρ_c depends approximately exponentially on mass,

$$\rho_c = 3.3 \times 10^7 e^{5.64 \times (m-1)} \text{g cm}^{-3},$$

where m is in solar masses. As very little mass is ejected during the simulation (the merger is essentially conservative), the coronal mass is:

$$m_{\text{corona}} = 0.81 \times e^{5.64 \times (m_2 - m_1)} \times m_1 \pm 0.03 \times m_1,$$

and

$$m_{\text{disk}} = m_2 - m_{\text{corona}}.$$

Although our calculations are for a CO+He WD merger, the masses are within the range of the Zhu et al. (2013) parameter space. We have therefore used this result to provide the coronal and disk masses in the eight models calculated for this paper and which are shown in Table 1.

Based on the corona-plus-disk model, a “destroyed – disk” model will be introduced in §7, in which the disk is assumed to be totally destroyed on a convective turnover timescale.

4 EVOLUTION TRACKS

In the SPH simulations of white dwarf mergers, matter in the hot corona may, for some models, briefly reach temperatures of $6 \times 10^8 \text{K}$ or more (Yoon et al. 2007; Lorén-Aguilar et al. 2009), so that some nucleosynthesis of α -rich material will occur. For models comparable to those calculated here, Zhu et al. (2013) find peak temperatures $\approx 1.74 - 2.47 \times 10^8 \text{K}$. Our one-dimensional quasi-equilibrium calculations indicate coronal temperatures up to $2.5 \times 10^8 \text{K}$ for all models after the fast accretion phase (see details in Fig. 3). At these temperatures, the 3α and other alpha-capture reactions are ignited at the surface of the accretor almost immediately. Thus, carbon is produced by helium burning and nitrogen is

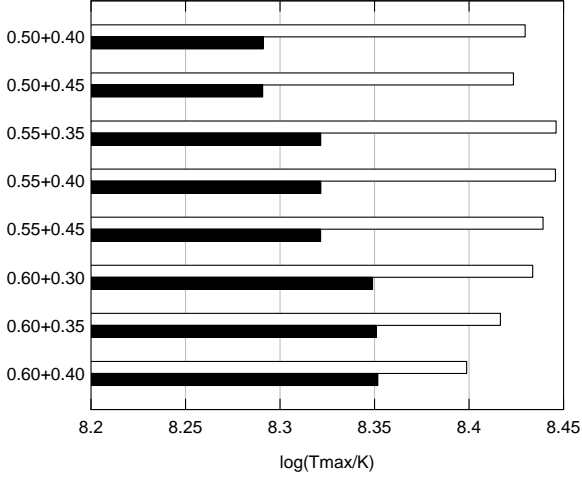


Figure 3. The maximum temperatures achieved in each of the ‘corona+disk’ merger models. The empty bar indicates the maximum temperature after the fast accretion phase. The filled bar indicates the maximum temperature after the slow accretion phase. The vertical axis labels identify each model by CO+He WD mass.

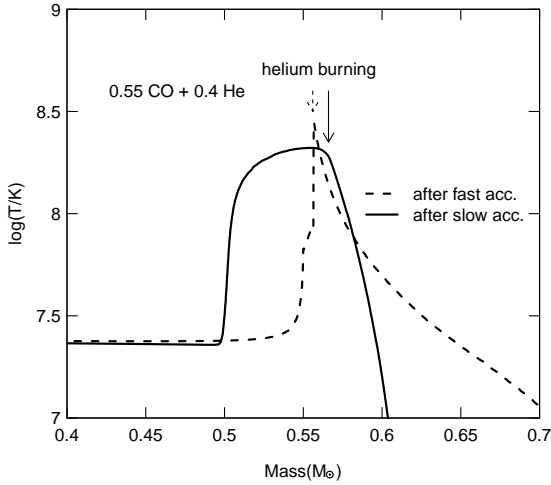


Figure 4. The temperature profile of model 0.55+0.40 M_{\odot} immediately after the fast accretion phase (dashed line) and after the slow accretion phase (solid). The arrows indicate the location of the center of 3α burning.

destroyed by α capture. As Warner (1967) and Clayton et al. (2007) indicated, the destruction of ^{14}N by the $^{14}\text{N}(\alpha, \gamma)^{18}\text{O}$ reaction becomes more efficient than it is at low temperature. As the temperature continues to increase, ^{18}O produces ^{22}Ne through an additional α capture. Because of the high accretion rate, there is no runaway helium flash and burning is stable. Most of the energy released during this process goes into heating the corona.

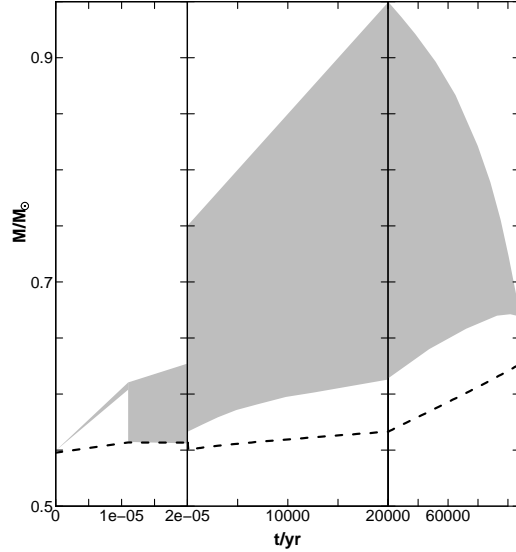


Figure 5. Convection regions during evolution (grey zone). Left: the location of convective regions during fast accretion of helium from a 0.40 M_{\odot} helium white dwarf onto 0.55 M_{\odot} carbon-oxygen white dwarf. The fast accretion rate is $10^4 M_{\odot}\text{yr}^{-1}$. Middle: the location of convective regions during the slow accretion of helium to the final mass 0.95 M_{\odot} . The slow accretion rate is $10^{-5} M_{\odot}\text{yr}^{-1}$. Right: the location of convective regions during the post-merger evolution of the 0.95 M_{\odot} product with mass loss via a Reimers'-type stellar wind ($\eta_R = 0.02$). The dashed line shows the helium-burning location.

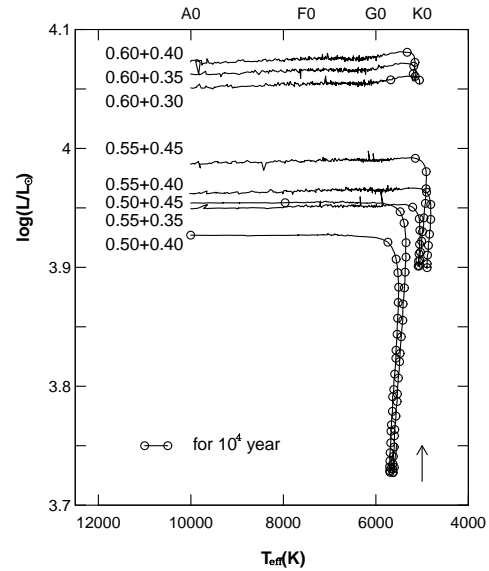


Figure 6. The $L - T_{\text{eff}}$ diagram showing post-merger evolution of all ‘corona+disk’ models. Circles represent intervals of 10^4 yrs. The arrow indicates the evolutionary direction, which is towards higher luminosity.

After the fast-accretion phase, slow accretion transfers matter from the disk to the accretor, whilst inward heat conduction from the helium-burning shell continues to heat the CO core. Meanwhile, the star starts to expand to become a red giant. After the slow accretion phase, the temperature maximum decreases, and the width of the hot shell increases. An example of the temperature profile of model 4 ($0.55+0.40 M_{\odot}$) at two different epochs is shown in Fig. 4.

The location of convective regions during the accretion and post-merger phases of model 4 ($0.55+0.40 M_{\odot}$) is shown in Fig. 5. After the fast accretion phase, the increasing nuclear luminosity forces the star to expand; the radius becomes about $210 R_{\odot}$ within 500 yrs. At this point, the envelope is almost fully convective, and helium-burning makes the corona rich in ^{12}C , ^{18}O and ^{22}Ne . The surface abundance of ^{12}C comes from the 3α reaction, which is very sensitive to temperature. However, during the (slow) disk-accretion phase the new ash of ^{12}C cannot reach the convection region, as shown in Fig. 5. Thus, all carbon enrichment occurs during the fast-accretion phase.

After the slow-accretion phase, the star becomes more luminous, and the mass-loss rate starts to become significant. The mass-loss rate depends on the Reimers' coefficient, and will be discussed in the next section.

As the helium shell burns outwards through the accreted envelope, and the wind removes mass from the surface, the helium envelope is eventually not massive enough to sustain a helium-burning shell, and the shell luminosity starts to drop. To compensate, the envelope shrinks and the star evolves to become a white dwarf, evolving to higher T_{eff} at constant luminosity. The evolution tracks for each model in the $L - T_{\text{eff}}$ diagram are shown in Fig. 6.

The evolution calculations were terminated when the contracting star reached $T_{\text{eff}} = 10\,000\text{ K}$. This limit is currently imposed by numerical instabilities associated with the extremely narrow helium-burning shell and the algorithm used by MESA to select an appropriate timestep. Work to overcome this limitation is in progress.

5 MASS LOSS AND DUST FORMATION

A carbon-rich dust environment is an important feature of RCB variables, the formation of which leads to the large visible brightness variations which are characteristic of the class. In our simulations, we assumed a Blöcker-type stellar wind (Blöcker 1995), of the type usually used to represent mass loss in AGB stars. For the longest-lived phase of our models, this gave a mass-loss rate $\sim 10^{-6} M_{\odot}\text{yr}^{-1}$, which is comparable with observational estimates (Clayton 2012). But this mass-loss rate is essentially determined by the Reimers' coefficient which has been set to $\eta_R = 0.02$ (see above). For $\eta_R = 0.1$, our model gave a mass-loss rate $\sim 10^{-5} M_{\odot}\text{yr}^{-1}$, and luminosity more than $\sim 1500 L_{\odot}$ lower than the $\eta_R = 0.02$ model. Details from the $L - T_{\text{eff}}$ diagram for the $0.55+0.40 M_{\odot}$ post-merger model are shown in Figs. 7 and 8, for $\eta_R = 0.02$ and 0.1 respectively. The $\eta_R = 0.02$ model loses $0.25 M_{\odot}$ within 8.4×10^4 yrs, and the $\eta_R = 0.1$ model loses $0.3 M_{\odot}$ within 2.5×10^4 yrs. Both models show small random changes of luminosity during mass loss. We repeated the evolution calculation for 20 years of the $\eta_R = 0.02$ model using different timesteps (Fig. 9). The

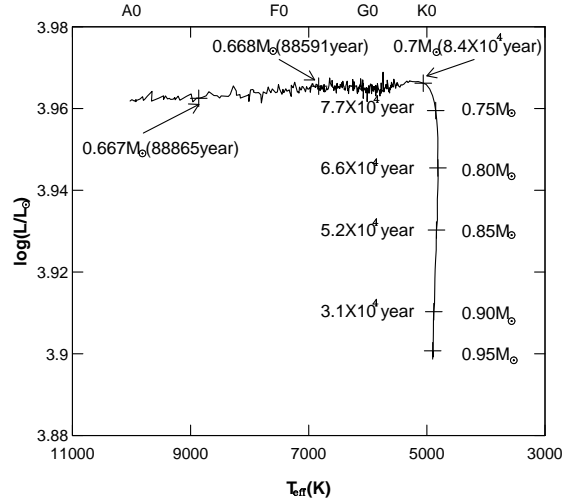


Figure 7. Detail of the $L - T_{\text{eff}}$ diagram for the $0.55+0.40 M_{\odot}$ post-merger model ($\eta_R = 0.02$). Times since the end of the slow-accretion phase and the total mass at those times are shown at key points on the track.

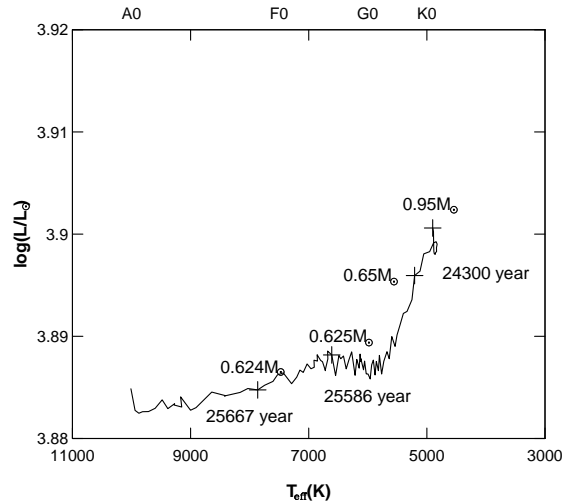


Figure 8. Detail of the $L - T_{\text{eff}}$ diagram for the $0.55+0.40 M_{\odot}$ post-merger model ($\eta_R = 0.1$). Times since the end of the slow-accretion phase and the total mass at those times are shown at key points on the track.

small-amplitude variations did not repeat themselves identically (although still present), so we conclude that this ‘noise’ is principally numerical.

In view of the observational constraints on mass-loss rate and luminosity provided by the RCB stars, we chose $\eta_R = 0.02$ for more detailed investigation. The evolution can be divided into two stages. During the first stage (A), the luminosity increases as the CO-core mass increases, with virtually no change in T_{eff} . In the following 5000 yrs (stage B),

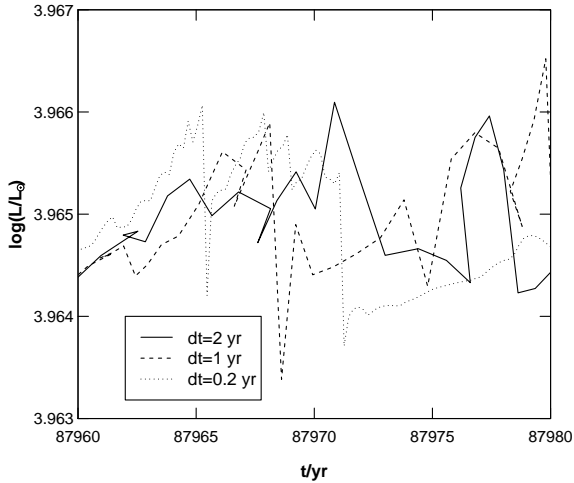


Figure 9. Detail of the luminosity changes for the $0.55+0.40 M_{\odot}$ post-merger model ($\eta_R = 0.02$). The solid, dashed and dotted lines for evolutionary tracks of timesteps of 2, 1 and 0.2 years respectively.

where the star contracts at constant luminosity (see above), the mass loss rate reduces to $6 \times 10^{-7} M_{\odot} \text{yr}^{-1}$, and the star loses a further $0.03 M_{\odot}$ to give a final mass $\approx 0.67 M_{\odot}$. We note that the mass is less than the estimate of $0.8 - 0.9 M_{\odot}$ from pulsation modeling (Saio & Jeffery 2002; Saio 2008), but that the mass-loss rate is higher than that estimated for EHe stars by Jeffery & Hamann (2010). If we assume a gas-to-dust ratio of 100 (Whittet 2003; Clayton 2012), we estimate that $\approx 2.5 \times 10^{-4} M_{\odot}$ of dust would be produced during stage A ($8.4 \times 10^4 \text{ yr}$).

6 SURFACE COMPOSITION

Fig. 10 shows that most of the RCB stars lie around the part of the post-merger evolution corresponding to the final contraction phase (stage B). To compare with our simulations, data on the chemical composition of 17 RCB and 2 EHe stars with $T_{\text{eff}} < 10000 \text{ K}$ have been taken from the compilation by Jeffery et al. (2011), which, in turn, was based on measurements by Asplund et al. (2000) and Pandey et al. (2008). Data for T_{eff} and surface gravities ($\log g$) of the same stars were taken from the latter two sources.

6.1 Individual elements

At the end of fast accretion and the beginning of slow accretion, flash-driven convection mixes ^{12}C throughout the envelope. During the subsequent slow-accretion phase, coronally-produced material is buried by C-poor material from the disk, so the new surface abundance very much depends on whereabouts in the star the disk material is deposited. In our simulations, which deposit disk material onto the surface of the accretor, only the models for a $0.55 M_{\odot}$ CO white dwarf merger with a helium white dwarf can produce a carbon-rich

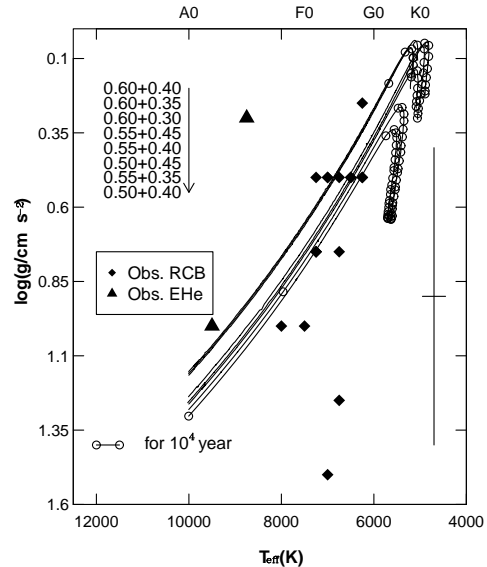


Figure 10. The surface-gravity – effective-temperature diagram for post-merger models. The diamonds show observed RCB stars. The triangles show observed EHe stars. The right cross shows an average error bar for the observations.

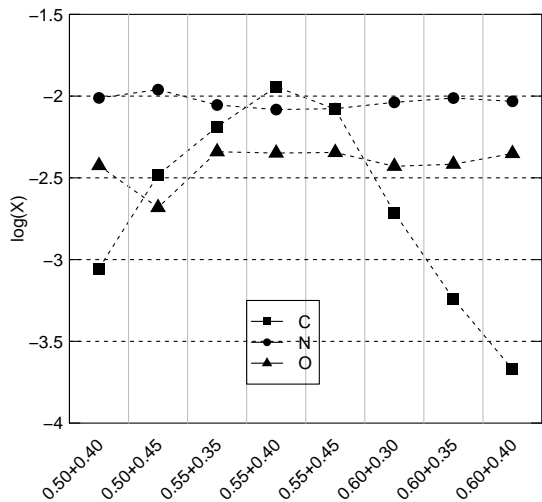


Figure 11. The surface carbon (squares), nitrogen (circles) and oxygen (triangles) abundances of each model.

surface; see Fig. 11 for details. All of the ^{12}C enrichment comes from the fast accretion phase as discussed above. The final carbon abundance depends on the peak temperature during accretion; in the models studied here, mergers onto a $0.55 M_{\odot}$ CO white dwarf show the highest surface carbon. This appears counter-intuitive. However, because of the larger mass ratio, the $0.60 M_{\odot}$ CO white dwarf accretes less mass during the fast merger phase, and hence the corona is cooler than in the $0.55 M_{\odot}$ case (Fig. 3), leading to the production of *less* carbon.

Table 2. Logarithmic mass fraction of carbon (β_C), nitrogen (β_N), oxygen (β_O), fluorine (β_F), neon (β_{Ne}), lithium (β_{Li}) and the number ratios for $^{12}C/^{13}C$, and $^{16}O/^{18}O$. Three models with accreted-hydrogen mass fractions $X = 0$ and $X = 0.0001$ are shown. Solar abundances are from Anders & Grevesse (1989).

Model	β_C	β_N	β_O	β_F	β_{Ne}	β_{Li}	$^{12}C/^{13}C$	$^{16}O/^{18}O$
$X = 0$								
0.55+0.35 M_{\odot}	-2.18	-2.05	-2.34	-7.47	-2.60	-7.25	284	0.56
0.55+0.40 M_{\odot}	-1.94	-2.08	-2.34	-7.26	-2.45	-7.11	497	0.60
0.55+0.45 M_{\odot}	-2.08	-2.07	-2.34	-7.21	-2.48	-7.05	360	0.57
$X = 0.0001$								
0.55+0.35 M_{\odot}	-3.04	-2.01	-2.46	-4.81	-2.66	-7.73	28	0.85
0.55+0.40 M_{\odot}	-3.08	-1.94	-2.80	-4.81	-2.73	-7.81	29	224
0.55+0.45 M_{\odot}	-2.30	-2.00	-2.77	-3.94	-2.39	-7.79	136	12
Solar	-2.51	-2.96	-2.02	-6.39	-2.76	-8.02	90	497

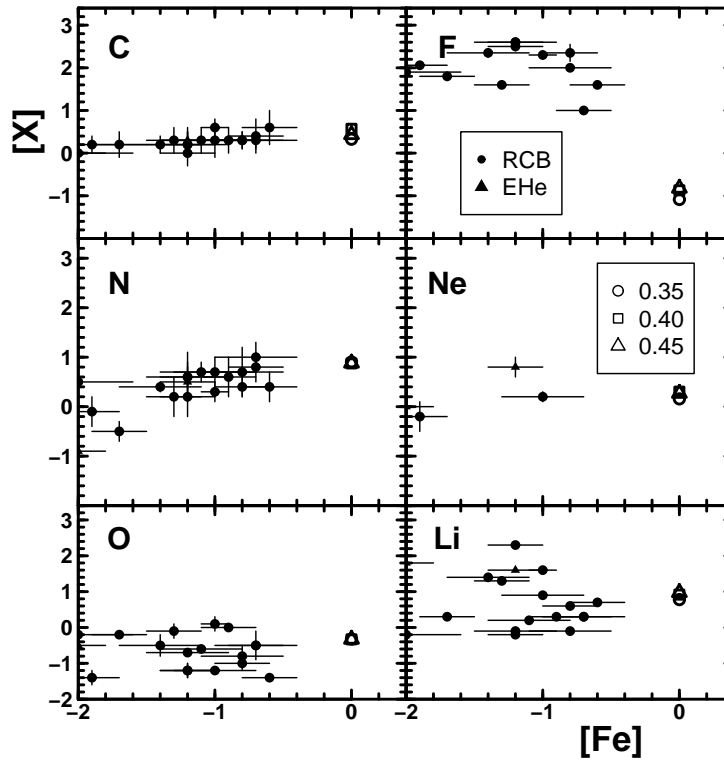


Figure 12. The observed surface abundances of RCB and EHe stars (Jeffery et al. 2011; Asplund et al. 2000; Pandey et al. 2008) compared with our nucleosynthesis computation (with accreted $X = 0$). The axes $[X]$ and $[Fe]$ give logarithmic abundances *by number* relative to solar (Anders & Grevesse 1989) for individual elements and for iron, respectively. Open circles, squares and diamonds are abundances given by our simulations for 0.55+0.35 M_{\odot} , 0.55+0.40 M_{\odot} and 0.55+0.45 M_{\odot} respectively.

Since we are concerned with the origin of the carbon-rich RCB stars, we focus our discussion on the three models producing most carbon, *i.e.* 0.55+0.35 M_{\odot} , 0.55+0.40 M_{\odot} and 0.55+0.45 M_{\odot} . The principal surface abundances arising from these models are shown in Fig. 12 and Table 2.

Carbon is enriched in all RCB stars. In those cool enough to show CO, the $^{12}C/^{13}C$ ratios are very large (≈ 500), indicating a 3α or helium-burning origin for the carbon excess. In our models, ^{12}C was produced by helium burning through

the 3α reaction during the hot accretion phase, and then brought up to the surface during the slow-accretion phase by flash-driven convection. The ^{13}C abundance remained almost unchanged during the whole simulation. This enrichment of ^{12}C results in a very high ratio of $^{12}C/^{13}C$, being 284, 497, and 360 in our simulation for models for 0.55+0.35 M_{\odot} , 0.55+0.40 M_{\odot} and 0.55+0.45 M_{\odot} , respectively. The total carbon, including ^{12}C and ^{13}C , shows an abundance similar to the observation (Fig. 12).

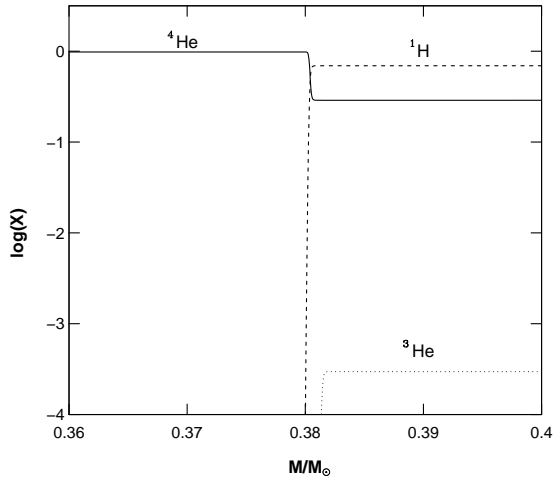


Figure 13. The abundance profile of a $0.4 M_{\odot}$ He white dwarf with a $0.02 M_{\odot}$ hydrogen envelope. The solid, dashed and dotted lines show ^4He , ^1H and ^3He , respectively.

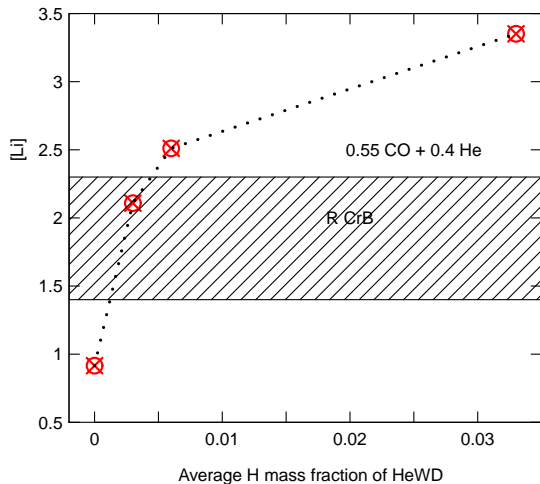


Figure 14. The abundance of Li produced during merger as a function of the hydrogen mass fraction in the accreted He white dwarf. The shaded zone shows the range of observed RCB lithium abundances.

Nitrogen is enriched in the RCB stars. Heber (1983) and subsequent authors point out that the N abundances in general follow the trend of the iron abundance. Nitrogen is enriched through CNO cycling in the parent stars. In our simulation, it is subsequently reduced by the $^{14}\text{N}(\alpha, \gamma)^{18}\text{O}$ reaction.

Oxygen is enriched in most RCB stars. Clayton et al. (2007) report that, for four RCBs, ^{18}O has a large enrichment and shows a low ratio of $^{16}\text{O}/^{18}\text{O}$ close to unity. By

comparison with the solar abundance, ^{18}O must have increased by a factor > 400 . Clayton et al. (2007) also indicate that the production of ^{18}O requires temperatures of at least 10^8 K to allow the $^{14}\text{N}(\alpha, \gamma)^{18}\text{O}$ reaction. ^{18}O is also produced by α -capture on ^{14}N during the fast-accretion phase in our models; the resulting $^{16}\text{O}/^{18}\text{O}$ ratios are 0.56, 0.60, and 0.57 for models $0.55+0.35 M_{\odot}$, $0.55+0.40 M_{\odot}$ and $0.55+0.45 M_{\odot}$, respectively. There is no *new* ^{16}O from alpha-capture during the fast-accretion phase.

Fluorine is enriched in most RCB stars by factors of 800–8000 relative to its probable initial abundance (Pandey et al. 2008). In our simulation, ^{19}F comes from the reaction $^{15}\text{N}(\alpha, \gamma)^{19}\text{F}$, but the quantity of ^{19}F produced is small. The newborn ^{19}F is mixed with disk-accreted material. As ^{19}F was destroyed by $^{19}\text{F}(p, \alpha)^{16}\text{O}$ during RGB evolution, the helium white dwarf is deficient in ^{19}F , having a mass fraction $\approx 8.5 \times 10^{-9}$ in our experiments. The fresh ^{19}F produced during the merger in our models is insufficient to match the observations.

Neon: a high overabundance of neon has been identified in several RCBs. In our simulation, ^{22}Ne is enriched by two α -captures on ^{14}N followed by extensive convective mixing.

Lithium: a few RCB stars have a notably large overabundance of lithium, which has so far been difficult to explain. Longland et al. (2012) show that lithium can be produced by the merging of a He WD with a CO WD if their chemical composition is rich in ^3He from the previous evolution. This model requires enough ^3He to be left in the white dwarf after the end of main-sequence evolution and a hot enough corona to form during the merger. In our simulation, we obtained a ^3He mass fraction of 7.7×10^{-8} in the He WD, which subsequently yielded a post-merger surface with a lithium mass fraction of 5.6×10^{-8} , 7.7×10^{-8} , and 8.8×10^{-8} for models $0.55+0.35 M_{\odot}$, $0.55+0.40 M_{\odot}$ and $0.55+0.45 M_{\odot}$, respectively, or about ten times solar. Hence it is clear that ^3He is the key to explain the RCB lithium abundances.

6.2 The rôle of the helium white dwarf envelope

According to stellar evolution theory, ^3He in a helium white dwarf is thought to be produced whilst the star was previously on the first giant branch where it is dredged into and remains in the hydrogen envelope (Benvenuto & Althaus 1998; Althaus & Benvenuto 2000; Althaus et al. 2001; Steinfadt et al. 2010; Longland et al. 2012). Thus, the more of the hydrogen envelope that survives from the giant to the helium white dwarf, the more ^3He it is expected to contain. The He WD envelope plays a very important rôle in nucleosynthesis during the merger, particularly with regard to the production of lithium and fluorine.

To test whether there is a relation between hydrogen abundance and lithium enrichment, we set another three $0.4 M_{\odot}$ He WDs, which have hydrogen envelope masses of 0.002 , 0.004 , $0.02 M_{\odot}$, to merge with a $0.55 M_{\odot}$ CO WD. The abundance profile of a $0.4 M_{\odot}$ He WD with a $0.02 M_{\odot}$ hydrogen envelope is shown in Fig. 13. We assumed that all coronal hydrogen would be destroyed in the very initial

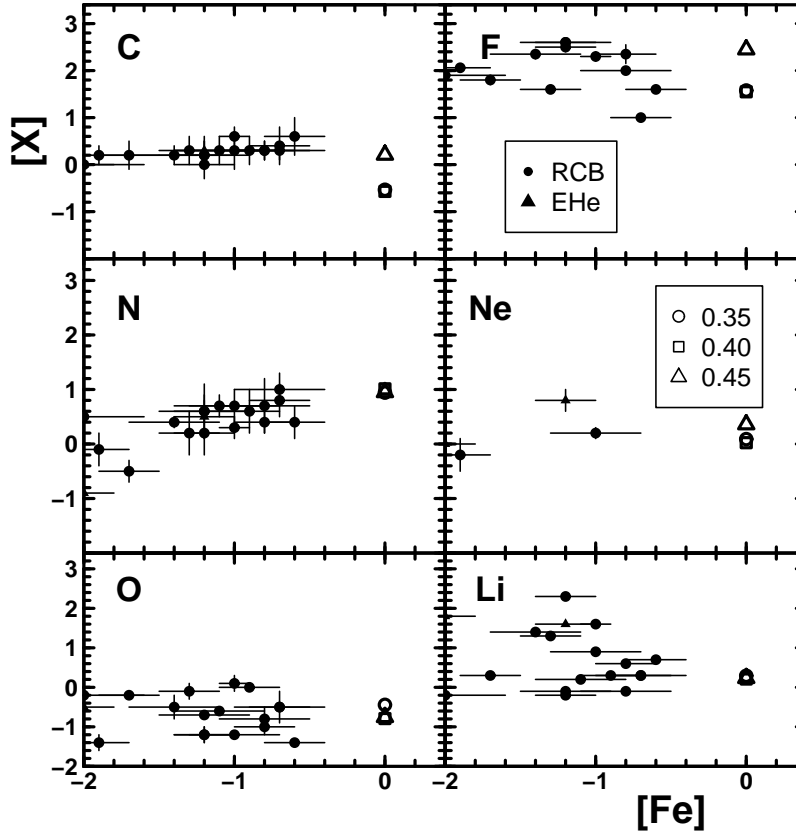


Figure 15. As Fig. 12, with hydrogen accretion ($X = 0.0001$). The observed surface abundances of RCB and EHe stars (Jeffery et al. 2011; Asplund et al. 2000; Pandey et al. 2008) compared with our nucleosynthesis computation. The axes $[X]$ and $[Fe]$ give logarithmic abundances *by number* relative to solar for individual elements and for iron, respectively. Open circles, squares and diamonds are abundances given by our simulations for models $0.55+0.35 M_{\odot}$, $0.55+0.40 M_{\odot}$ and $0.55+0.45 M_{\odot}$, respectively.

stage of the fast-accretion phase, and so set this phase to be hydrogen free ($X = 0$), but maintained the contribution from ${}^3\text{He}$. Without this assumption (i.e. with $X \neq 0$), stable helium-burning could not be achieved during the accretion phase. Hydrogen which is not destroyed immediately at the beginning of accretion will be completely mixed in the accretion materials and may survive in both the disk and outer envelope. In a second experiment, we therefore tested the inclusion of a hydrogen mass fraction $X = 0.0001$ during both accretion phases.

As shown in Fig. 15 and Table 2, the abundances for nitrogen, neon and oxygen are similar to models without hydrogen. The carbon abundance is lower in models including hydrogen than in models without hydrogen. Carbon is decreased by the ${}^{12}\text{C}(p, \gamma){}^{13}\text{N}(\beta^+ \mu){}^{13}\text{C}(p, \gamma){}^{14}\text{N}$ reaction in all models where hydrogen is present in the accreted material. At the same time, the ${}^{12}\text{C}/{}^{13}\text{C}$ ratio is also decreased and does not agree with observation. Hence the observed ${}^{12}\text{C}/{}^{13}\text{C}$ ratios limit the amount of hydrogen that can be present in the accreted material.

The more massive the hydrogen envelope in the helium white dwarf, the more ${}^3\text{He}$ it contains, and hence the more lithium is produced in the merger (Fig. 14).

The inclusion of a small quantity of hydrogen also affects the final fluorine abundances via the proton capture

reaction ${}^{18}\text{O}(p, \gamma){}^{19}\text{F}$. Since a surplus of ${}^{18}\text{O}$ is produced during the hot coronal phase, and only a small quantity of ${}^{19}\text{F}$ is required to substantially alter the initial abundances, this mechanism can explain the fluorine excesses observed in RCB and EHe stars (Pandey et al. 2006, 2008).

The above tests demonstrate that a hydrogen envelope on the helium white dwarf readily explains the enrichment of both ${}^7\text{Li}$ and ${}^{19}\text{F}$. The abundance of ${}^7\text{Li}$ depends on the fraction of ${}^3\text{He}$ in the hydrogen envelope; and the abundance of ${}^{19}\text{F}$ depends on the fraction of ${}^1\text{H}$ in the accreted material.

7 DISK DESTRUCTION

If we only consider evolution after the fast-accretion phase, the star will expand to become a giant on a short timescale. For instance, the $0.55+0.20 M_{\odot}$ merger model expands to a radius of $\sim 210 R_{\odot}$ within 500 years (Fig. 16).

SPH simulations show the debris disks to be smaller than $0.1 R_{\odot}$ (Yoon et al. 2007; Lorén-Aguilar et al. 2009; Longland et al. 2012; Zhu et al. 2013; Dan et al. 2014). The envelope becomes almost fully convective when expanding, and hence the Keplerian disk may well be destroyed by convection and other mixing processes. Driven by helium-burning at its base, the convection region of the envelope will expand to $0.1 R_{\odot}$ within 0.1 years (Fig. 17). If the disk is

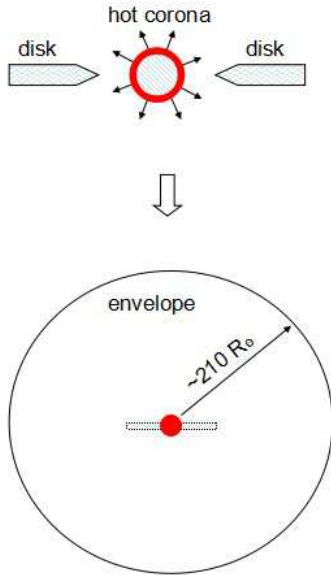


Figure 16. Cartoon illustrating possible envelope expanding phase of merger.

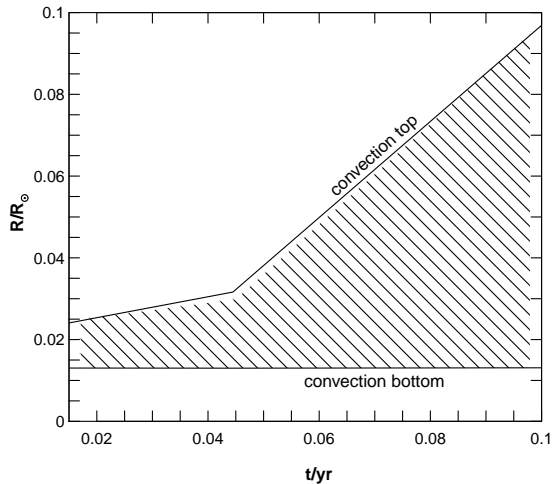


Figure 17. Radius evolution of the convection zone of a $0.55+0.40 M_{\odot}$ destroyed-disk merger model immediately following the fast accretion phase.

assumed to be totally destroyed by convection, the accretion rate will be $2 M_{\odot} \text{ yr}^{-1}$. We adopt this accretion rate to make a new class of post-merger model, which we call “destroyed disk” models, and evolve these models with $\eta_R = 0.02$ stellar winds, and hydrogen-free ($X = 0$) accretion.

In order to consider both destroyed-disk and low- q mergers, we produced 15 models comprising 0.50 , 0.55 , and $0.6 M_{\odot}$ CO WDs merging with 0.20 , 0.25 , 0.30 , 0.35 , and $0.40 M_{\odot}$ He WDs. We set the mass-accretion rate to be $2 M_{\odot} \text{ yr}^{-1}$ to emulate the disk-destruction process.

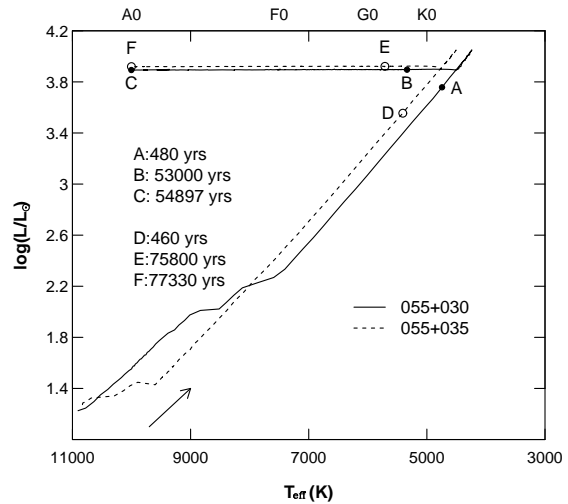


Figure 18. Evolutionary tracks of two destroyed-disk models. The solid and dashed lines for $0.55+0.30$ and $0.55+0.35 M_{\odot}$ models with $\eta_R = 0.02$, respectively. Letters A–C and D–F indicate times since merger for each of the two tracks.

7.1 Hertzsprung-Russell diagram

The post-merger evolutionary tracks of two destroyed-disk models with different masses are shown in Fig. 18. After the merger process, they take ~ 500 years to expand to the giant position. After the Reimers’ wind has removed most of the mass from the envelope (typically $\approx 70\%$), shell-helium burning makes the star evolve to high temperature without a luminosity change, as in most post-AGB stars. Taking the $0.55+0.30 M_{\odot}$ model, for instance, the star takes 480 years to expand to $112 R_{\odot}$ (marked A on Fig. 18) and only loses $3.3 \times 10^{-6} M_{\odot}$. Evolution from A to B takes 52 520 years, with a loss of $0.22 M_{\odot}$, and the radius only decreases to $103 R_{\odot}$. Evolution from stage B to C takes 1897 years and the temperature increases from 5336 K to 10000 K.

7.2 Comparison with observation

The locations of seventeen RCB and two EHe stars with $T_{\text{eff}} < 10\,000 \text{ K}$ on the temperature-gravity diagram are compared with the destroyed-disk post-merger evolution tracks (Fig. 19). In this figure, most RCB stars lie around the part of the post-merger evolution corresponding to the final contraction phase (B to C).

7.3 Abundances

Table 3 shows that the surface carbon abundance varies with mass. We also find enhanced abundances of N, O, Ne, and Li. All of these elements are compared with observed RCB and EHe stars in Fig. 21. Fluorine is low because there was no hydrogen in the accreted material. These calculations show that carbon is, again, only enhanced to the degree observed in models where the CO WD has a mass $\approx 0.55 M_{\odot}$. However, high surface carbon is achieved for *lower* He WD

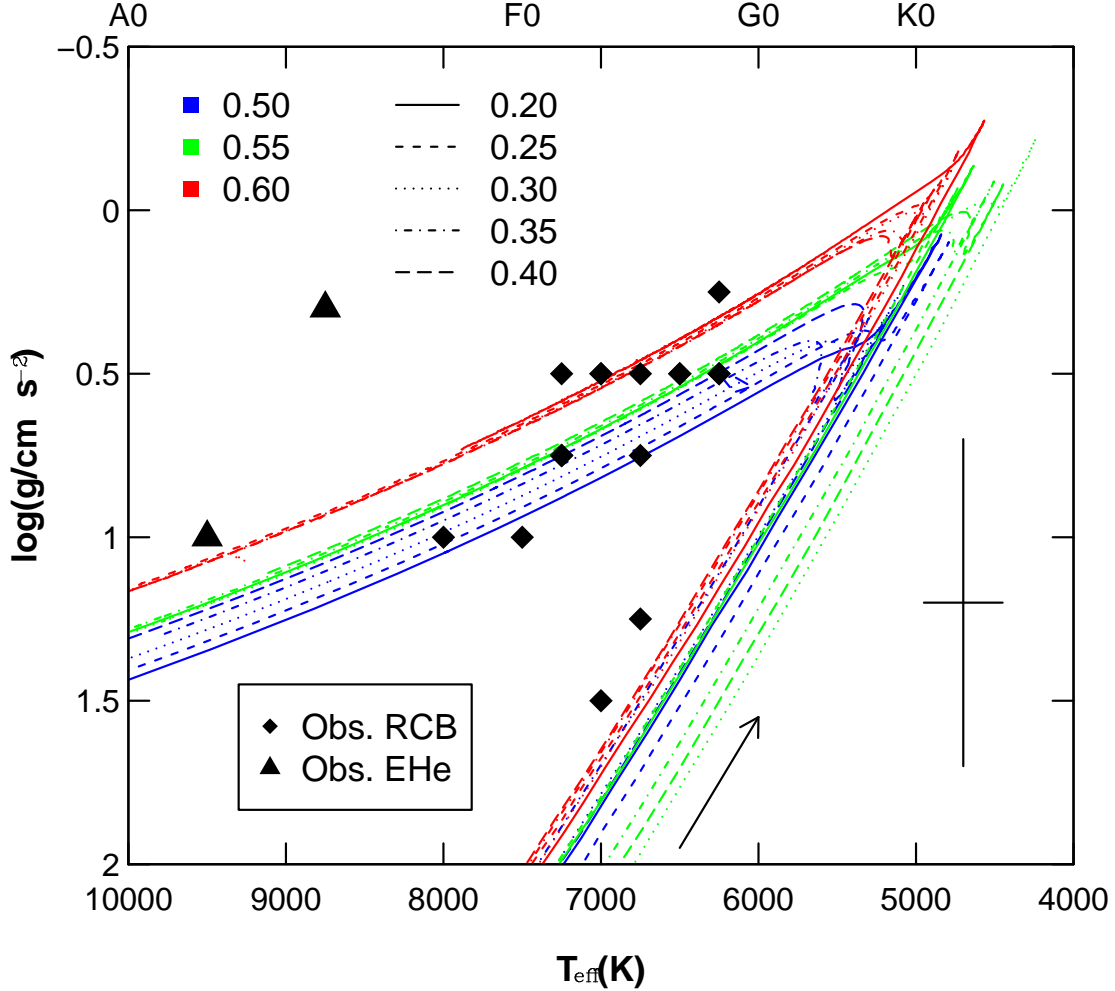


Figure 19. The surface gravity – effective temperature tracks for destroyed-disk post-merger models. Different colours identify different CO WD masses, *i.e.* blue for 0.50 M_{\odot} , green for 0.55 M_{\odot} and red for 0.60 M_{\odot} . Different line styles identify different He WD masses, *i.e.* solid for 0.20 M_{\odot} , dashed for 0.25 M_{\odot} , dotted for 0.30 M_{\odot} , dash-dotted for 0.35 M_{\odot} , and long-dashed for 0.40 M_{\odot} . The arrow indicates the evolutionary direction, which is initially towards lower gravity. The diamonds show observed RCB stars. The triangles show observed EHe stars with $T_{\text{eff}} < 10000\text{K}$. The cross at the lower right shows the average error in the observations.

masses, *i.e.* $\geq 0.30 M_{\odot}$, than in the models presented in §4–6.

The slow-neutron capture process (s-process) occurs at temperatures $T > 2.2 - 3.5 \times 10^8 \text{K}$ and $\rho > 1 - 3 \times 10^3 \text{g/cm}^3$ (Raiteri et al. 1991; Meyer 1994). The temperature and density of the burning shell in our models satisfies this condition. In the destroyed-disk model, convection completely mixes the outer layers of the star so that any s-processed material produced in the shell during the merger and/or disk ingestion will become visible on the surface (Fig. 20). However, s-process nucleosynthesis is not included in the version of MESA used in these calculations, so we are not in a position to make a comparison with the observational constraints.

8 PULSATION

Following a series of studies of pulsation in hydrogen-deficient stars, Jeffery & Saio (2013) extended their stability calculations as a function of hydrogen abundance (mass fraction: X) to a larger range of effective temperature (T_{eff}), luminosity-to-mass ratio (L/M) and X than before (Jeffery & Saio 1999). Fig. 22 shows a fragment of the instability domain for $X = 0.002$ and solar metallicity. At low T_{eff} the classical “Cepheid” instability strip is evident, although shifted to higher T_{eff} because of the reduced surface hydrogen. At high L/M strange modes are excited. The strange modes are less sensitive to X , and correspond to the observed locations of the variable RCB

Table 3. Post-merger surface abundances for disk-destroyed models with accreted $X = 0$. The table shows logarithmic mass fractions β of carbon (β_C), nitrogen (β_N), oxygen (β_O), fluorine (β_F), neon (β_{Ne}), lithium (β_{Li}) and the number ratios for $^{12}\text{C}/^{13}\text{C}$, and $^{16}\text{O}/^{18}\text{O}$. Solar abundances are from Anders & Grevesse (1989).

Model (CO+He)	β_C	β_N	β_O	β_F	β_{Ne}	β_{Li}	$^{12}\text{C}/^{13}\text{C}$	$^{16}\text{O}/^{18}\text{O}$
0.50+0.20 M_\odot	-2.23	-2.16	-2.20	-7.31	-2.49	-6.94	259	0.35
0.50+0.25 M_\odot	-2.09	-2.14	-2.20	-7.28	-2.53	-6.87	361	0.35
0.50+0.30 M_\odot	-2.50	-2.17	-2.13	-7.58	-2.65	-6.75	140	0.28
0.50+0.35 M_\odot	-3.24	-2.04	-2.32	-7.94	-2.79	-6.75	24	0.51
0.50+0.40 M_\odot	-2.32	-1.96	-2.68	-7.55	-2.65	-6.93	208	3.12
0.55+0.20 M_\odot	-2.27	-2.22	-2.19	-7.28	-2.34	-6.98	235	0.34
0.55+0.25 M_\odot	-2.46	-2.41	-1.99	-7.41	-2.47	-6.81	151	0.19
0.55+0.30 M_\odot	-1.69	-2.26	-2.26	-6.83	-2.17	-6.78	891	0.45
0.55+0.35 M_\odot	-1.89	-2.12	-2.25	-7.19	-2.47	-6.75	571	0.43
0.55+0.40 M_\odot	-1.78	-2.08	-2.34	-7.16	-2.46	-6.75	735	0.60
0.60+0.20 M_\odot	-2.42	-2.21	-2.16	-7.45	-2.42	-7.07	164	0.31
0.60+0.25 M_\odot	-3.04	-2.22	-2.09	-7.77	-2.57	-6.97	39	0.25
0.60+0.30 M_\odot	-2.81	-2.16	-2.15	-7.58	-2.62	-6.94	66	0.30
0.60+0.35 M_\odot	-3.55	-2.06	-2.27	-7.95	-2.78	-6.94	11	0.43
0.60+0.40 M_\odot	-3.75	-1.98	-2.50	-8.01	-2.82	-6.89	6	1.03
Solar	-2.51	-2.96	-2.02	-6.39	-2.76	-8.02	90	497

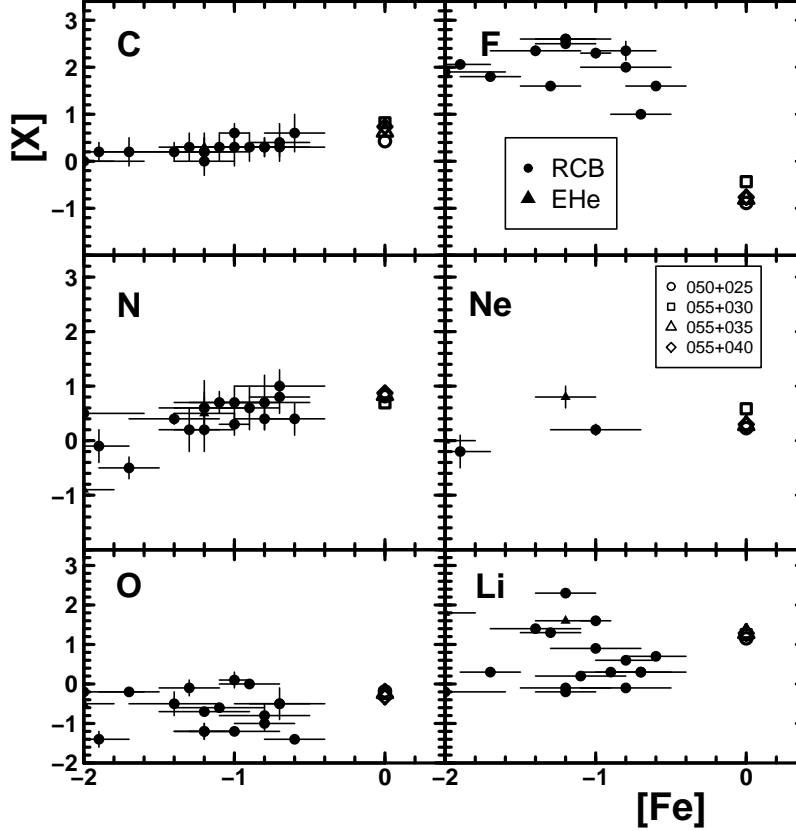


Figure 21. The observed surface abundances of RCB and EHe stars (Jeffery et al. 2011; Asplund et al. 2000; Pandey et al. 2008) compared with our nucleosynthesis computation for destroyed-disk models (accreted $X = 0$). The axes $[X]$ and $[Fe]$ give logarithmic abundances *by number* relative to solar (Anders & Grevesse 1989) for individual elements and for iron, respectively. Open circles, squares, triangle and diamonds are abundances for the 0.55+0.25, 0.55+0.30 M_\odot , 0.55+0.35 M_\odot and 0.55+0.40 M_\odot models, respectively.

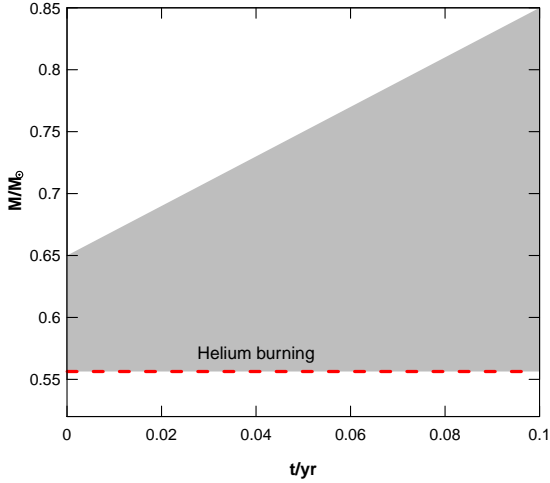


Figure 20. Convection boundaries during the early evolution of the $0.55+0.30 M_{\odot}$ destroyed-disk model.

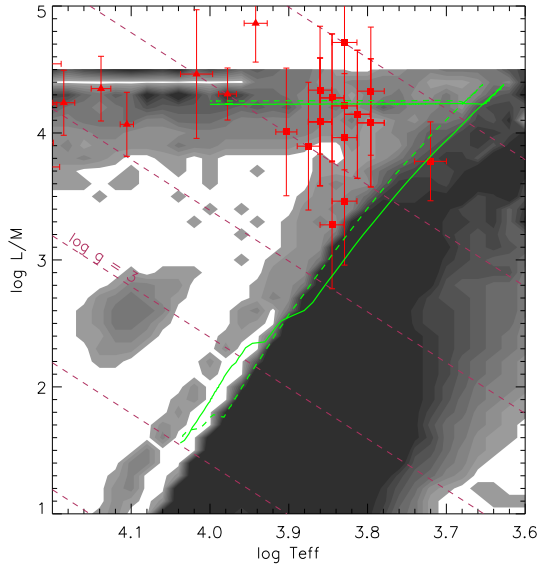


Figure 22. A grey-scale contour plot showing the number of unstable radial modes with $n < 15$ in linear non-adiabatic pulsation analyses of hydrogen-deficient stellar envelopes. The ordinate is $\log L/M$ in solar units, and the abscissa is $\log T_{\text{eff}}$. The plot is virtually invariant to the mass, at least in the range $0.2 - 1.0 M_{\odot}$. The solid squares correspond to EHe stars, triangles to RCB stars. White means there are no unstable modes, except for $\log L/M > 4.5$, where model envelopes are difficult to compute. Black means 15 or more unstable modes. Surface gravity contours for $\log g = 5, 4, 3, \dots$ are represented as broken lines. Evolution tracks for two destroyed-disk post-merger models are superimposed (green): $0.55+0.30 M_{\odot}$ (solid) and $0.55+0.35 M_{\odot}$ (broken). (Adapted from Jeffery & Saio (2013)).

and EHe stars. Strange-mode oscillations in stars with high L/M ratios have been identified for some time (Wood 1976). They appear theoretically in non-adiabatic pulsation analyses and have no corresponding modes in the adiabatic approximation. In particular, they appear to be associated with stellar envelopes where high opacities in the ionisation zones also lead to a density inversion – effectively creating a radiation-pressure dominated cavity in the stellar interior. They are discussed at greater length by, *inter alia*, Gautschy & Glatzel (1990) and Saio et al. (1998).

The evolution tracks for CO+He WD mergers lie entirely within the unstable domain, with pulsation in classical radial modes driven by the second helium ionization zone at low T_{eff} , and in strange modes at high L (Fig. 22).

9 POPULATION SYNTHESIS

The birthrate of RCB stars from the merger of CO+He WD binaries has been estimated using a binary population synthesis technique. We perform a Monte-Carlo simulation to obtain a population of primordial binaries, then evolve each binary using a rapid binary evolution code (RBEC) (Hurley et al. 2000, 2002) to obtain samples of double WD binaries. In the Monte Carlo simulation, all stars are assumed to be members of binaries and have circular orbits, while the primaries are generated according to the formula of Eggleton et al. (1989), *i.e.* following the initial mass function of Miller & Scalo (1979) and in the mass range 0.08 to $100 M_{\odot}$. The secondary mass, also with a lower limit of $0.08 M_{\odot}$, is then obtained assuming a constant mass-ratio distribution. The distribution of orbital separations, $an(a)$, is taken to be constant in $\log a$ for wide binaries and falls off smoothly at small separations according to Eq. (12)¹ in Han (1998), implying an equal number of wide binary systems per logarithmic interval and approximately 50% of stellar systems with orbital periods less than 100 yr (Han 1998).

The numbers and characteristics of double WD binaries significantly depend on the critical mass ratio for dynamical instability $q_c (= m_2/m_1)$ and common-envelope (CE) evolution (Han 1998). Here we adopt equation (57)² of (Hurley et al. 2002) for q_c when the mass donor is on the first or asymptotic giant branch (AGB), and use the standard energy formalism (van den Heuvel 1976; Webbink 1984; Livio & Soker 1988) for CE evolution by setting $\lambda\alpha_{\text{ce}} = 1.5$ which reproduces the number of the double WD binaries in the Galaxy as in previous studies (Wang et al. 2009).

Fig. 23 shows the rates of possible mergers from CO+CO, CO+He and He+He WD binaries for a single star-burst (normalized to $10^{11} M_{\odot}$). These include only mergers arising from WD binaries which fill their Roche lobes in a Hubble time. If $q < q_c$, mass transfer may be stable and may not produce a merger immediately. The CO+He systems

¹ for $a \leq a_0$, $an(a) = 0.070(a/a_0)^{1.2}$; for $a_0 \leq a \leq a_1$, $an(a) = 0.070$, where $a_0 = 10 R_{\odot}$, $a_1 = 5.75 \times 10^6 R_{\odot} = 0.13 \text{ pc}$.

² for a normal giant, the mass-radius relation $R \propto m^{-x}$ is assumed. Thus $q_c = [1.67 - x + 2(m_{\text{c1}}/m_1)]/2.13$, where m_{c1} is core mass of m_1 .

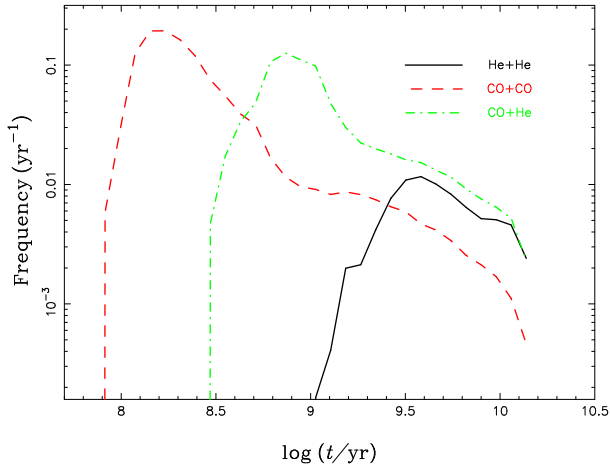


Figure 23. Frequency of possible mergers from CO+CO, CO+He and He+He WD systems for a single starburst (normalized to $10^{11} M_{\odot}$). The systems are assumed to have merged when the larger components fill their Roche lobes. The three types of white-dwarf merger are labelled.

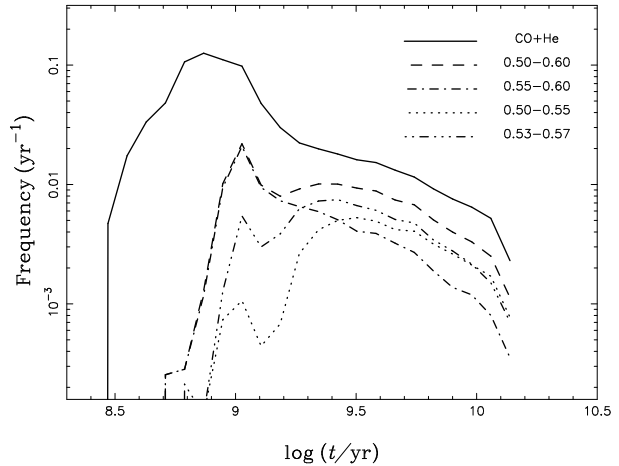


Figure 25. Frequency of RCB stars from CO+He mergers for various ranges of the CO WD mass and for a single starburst normalized to $10^{11} M_{\odot}$. CO+He refers to all possible CO+He mergers as shown in Fig. 23.

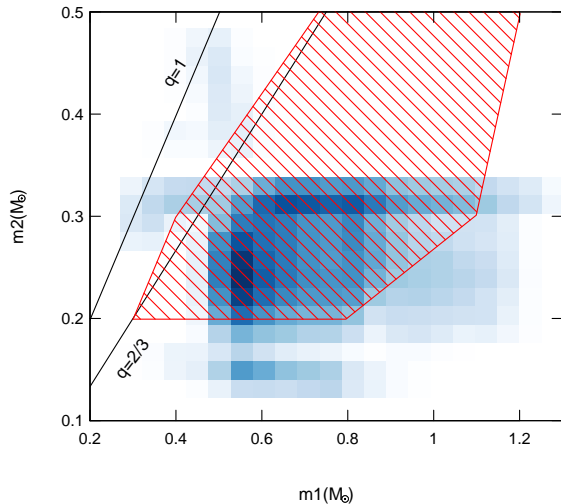


Figure 24. The relative number of CO+He binaries in the $M_{\text{CO}} - M_{\text{He}}$ plane is illustrated in this colour-density plot, where m_1 represents CO WDs, and m_2 represents He WDs. Otherwise the figure is similar to Fig. 1. The hatched region marks the area studied by Dan et al. (2011). The colour-density scale is linear, with the darkest shading corresponding to 3000 CO+He WD binaries per cell in the $10^{11} M_{\odot}$ simulation. The sample comprises 345371 WD pairs.

are produced from stable RLOF+CE³ or CE+CE interactions to be sure that the orbital separation is small enough and the systems can merge in a Hubble time. The He WDs *must* be formed in the second CE process. The binding energy of an AGB-star envelope (with a CO core) is small, so that CE ejection results in an orbital separation too wide to merge in a Hubble time if the CO WD forms *after* the

He WD. Furthermore, the smaller the mass of the He WD, then the larger the binding energy of the envelope and the more orbital energy is required and used for CE ejection. Thus the CO+He binaries which have the shortest periods and hence the highest likelihood to merge will be those containing the lowest mass He-WDs. Consequently, most of the merged CO+He binaries in Fig. 23 have low-mass He companions before merger. Fig. 24 shows a number-density plot for CO+He WD binaries in the $M_{\text{CO}} - M_{\text{He}}$ plane. If we adopt the critical mass ratio for dynamically unstable mass transfer to be $q > 0.6$ (Motl et al. (2007) give 0.67), Fig. 24 suggests that relatively few RCBs will be produced from CO+He WD mergers.

As discussed in §2, mass transfer in many low mass-ratio binaries is probably unstable and super-Eddington accretion may occur (Fig. 1: hatched region). Indeed, Dan et al. (2011) find a weak coupling between spin and orbit that leads almost all systems with $q \gtrsim 0.2$ to merge. In our calculations, the ^{12}C abundance of RCBs can only be explained if $M_{\text{CO}} \approx 0.55 M_{\odot}$. In this case, mass transfer is unstable if $M_{\text{He}} > 0.2 M_{\odot}$. We have computed the RCB birthrate for various ranges of the CO WD mass, i.e. for $M_{\text{CO}} = 0.5 - 0.6$, $0.55 - 0.6$, $0.5 - 0.55$ and $0.53 - 0.57 M_{\odot}$ (Fig. 25). These show that RCBs appear at about 10^9 yr after a single starburst, and the peak frequency is $\approx 0.02 \text{ yr}^{-1}$ for the optimum range of CO WD mass ($0.5 - 0.6 M_{\odot}$). The dip around 1.3 Gyr separates double WD binaries produced by the stable RLOF+CE process, which dominate at long lifetimes, from the more compact double WD systems produced by the CE+CE process, which dominate at short lifetimes. CO WDs with masses of $0.55 - 0.60 M_{\odot}$ account for the formation of RCBs when $t < 2$ Gyr, while those with masses of $0.50 - 0.55 M_{\odot}$ dominate RCB production for longer lifetimes.

Fig. 25 represents the formation rate from a single starburst, as possibly represented by the old population of the galactic bulge to which RCBs and EHes are believed to belong. The theoretical merger lifetimes are too short to explain the current numbers of RCBs and EHes in this way. Sufficient numbers of CO+He WD binaries can only come

³ RLOF = Roche Lobe Overflow

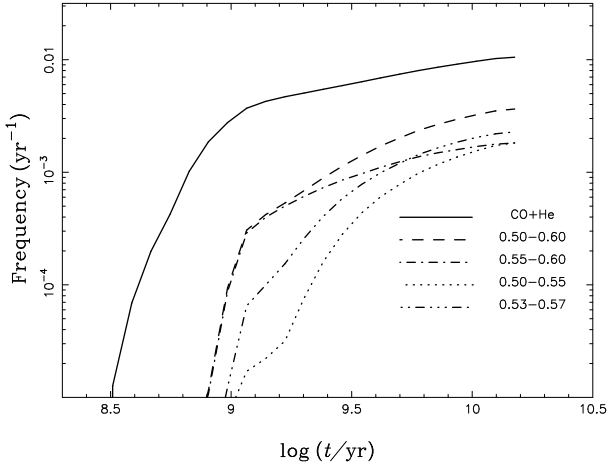


Figure 26. As Fig. 25 for a constant star formation rate of $5 \text{ M}_{\odot}/\text{yr}$ over the past 15 Gyr.

from relatively recent (≤ 2 Gyr) star formation. Fig. 26 shows the merger rates for a similar calculation assuming a constant star-formation rate of $5 \text{ M}_{\odot} \text{ yr}^{-1}$ over the past 15 Gyr, resembling the Galactic disk. The RCB birthrate in this simulation is 0.0036 yr^{-1} at 15 Gyr for the optimum case ($0.55 - 0.60 \text{ M}_{\odot}$), enough to explain the number of RCBs in our Galaxy.

In our post-merger evolution models, the timescales of the RCB stages are $\approx 50\,000$ to $70\,000$ yrs. Assuming a birthrate of 0.003 yr^{-1} gives $\approx 170 - 250$ RCB stars in the Galaxy. As the timescale for the EHe stage is less than 10% of the RCB stage, the number of EHes will be $\approx 17 - 25$. Current observations give 68 known active RCBs and 17 known EHes in the Galaxy. It is not clear what fraction of stars in the theoretical RCB stage will be active in the sense of showing RCB-type minima, or what the overall completeness statistics are. The predicted and observed numbers are comparable within these unknowns.

10 CONCLUSION

The merger of a helium white dwarf with a carbon-oxygen white dwarf in a short-period binary currently provides the preferred model for the origin of RCB stars. Guided by hydrodynamical calculations of the dynamical merger, which provide approximate initial conditions for the subsequent evolution, we have made one-dimensional calculations of the post-merger evolution. We have considered the separate contributions of the hot corona and cold Keplerian disk which are formed from the helium white dwarf, and have also considered the chemistry of the helium white dwarf.

We have calculated how the luminosity and effective temperature of the star evolve over time, and also how the surface composition behaves in response to the chemistry of the progenitor white dwarfs, to nucleosynthesis during and after the merger, to disruption of the helium white dwarf and to convective mixing during the post-merger evolution. We have included mass-loss assuming a Böcker-type stellar wind, and have considered the effects of enhancing this wind as a consequence of the hydrogen-deficient carbon-rich chemistry. Following merger, the stars become luminous and

spend some 50 000 to 70 000 yrs in the domain of the RCB variables, where their surface chemistries strongly resemble those observed. Our calculations suggest that the observed ^{12}C abundances can only be produced by a very small range in the mass of the CO white dwarf around $0.55 \pm 0.02 \text{ M}_{\odot}$. As found previously, ^{18}O is produced during and survives the merger to account for observed overabundances of oxygen. Some ^{18}O , reacting with hydrogen from the helium white dwarf, and ^3He from the same source, combining with ^4He , can account for the enrichment of fluorine and lithium seen in many RCB stars.

To account for the small-size of the Keplerian disk relative to the expanding star, and its likely ingestion into that envelope, we have investigated a new class of model, the “destroyed-disk” model, in which the disk is assumed to be totally destroyed on a convective turnover timescale. A CO WD mass of $0.55 \pm 0.02 \text{ M}_{\odot}$ is still required to produce high surface carbon, but a lower range in the He WD mass is permissible ($\geq 0.30 \text{ M}_{\odot}$).

The post-merger evolution tracks pass through a region of the $L - T_{\text{eff}}$ diagram where stars are predicted to be pulsationally unstable, as is generally observed. Binary population synthesis (BPS) calculations indicate that the highest fraction of CO+He WD binaries have masses of around 0.55 (CO) and 0.25 (He) M_{\odot} respectively. Combining the evolution timescales with estimates of merger rates from the BPS calculations yields an estimate of present-day numbers consistent with current observation.

A few problems still need to be addressed: i) post-merger evolution calculations and observed carbon abundances require the He WD masses to be in the range 0.30 M_{\odot} (destroyed-disk) to 0.45 M_{\odot} (fast+slow) whereas BPS simulations show most He-WD companions have masses in the range $0.2 - 0.3 \text{ M}_{\odot}$, ii) observed luminosities and evolution calculations imply total masses around $0.8 - 1.0 \text{ M}_{\odot}$, whereas BPS simulations favour total masses in the range $0.75 - 0.85 \text{ M}_{\odot}$ (with some outliers in both cases), iii) the BPS calculations imply that spin-orbit coupling must be weak so as to allow dynamical mergers for $0.5 < q < 0.67$, and iv) the observed distribution of Galactic RCB stars must be reconciled with a relatively young (< 2 Gyr) stellar population. The first three might readily be solved by considering in detail the rôle of spin-orbit coupling as suggested in §9, and by Dan et al. (2011). Accurate measurements of distances, luminosities and masses will provide crucial tests for the models, whilst work on the effect of rotation and the distribution of angular momentum following merger will have important consequences for interpreting the products.

A number of RCB observables have not been considered in the current paper. The ejection of carbon-rich material from the system either during the merger or in the form of an enhanced Böcker-type wind may lead to the formation of a circumstellar shell. Cool dust shells are observed to exist around several RCB stars. A comparison of the observed masses and sizes with what might be expected theoretically would be valuable. It would be interesting to know whether the shells were formed during the stage A phase (as ejecta from the dynamical merger) or during the subsequent stage B evolution. More theoretical work on how mass-loss works in these stars would also be useful, particularly in reconciling the *ad hoc* use of a Böcker-type wind with the episodic dust ejection associated with RCB variability.

In §6 we noted that CO+He WD mergers may also result in stars that are *not* carbon-rich. One may speculate upon how such stars might appear and whether they could be recognised. The evolution tracks continue to imply a passage through the AGB and post-AGB regions of the $L - T_{\text{eff}}$ plane. With reduced carbon, the characteristic dust-ejection episodes and the molecular C_2 (Swan) absorption bands would be absent. The surface chemistry would remain hydrogen-deficient, so CH and OH would not be strong, but other signatures such as lithium and fluorine could persist. More detailed computations of the surface chemistry, based, for example, on the calculations presented here, would be worthwhile.

ACKNOWLEDGMENTS

The Armagh Observatory is supported by a grant from the Northern Ireland Dept. of Culture Arts and Leisure. Z.H. is partly supported by the Natural Science Foundation of China (Grant Nos 11390374 and 11033008), the Science and Technology Innovation Talent Programme of the Yunnan Province (Grant No. 2013HA005) and the Chinese Academy of Sciences (Grant No. XDB09010202). X.C. is partly supported by the Natural Science Foundation of China (Grant No. 11173055), the Talent Project of Young Researchers of Yunnan Province (2012HB037) and the Chinese Academy of Sciences.

REFERENCES

- Alcock C., Allsman R. A., Alves D. R., Axelrod T. S., Becker A., et al. 2001, *ApJ*, 554, 298
- Althaus L. G., Benvenuto O. G., 2000, *MNRAS*, 317, 952
- Althaus L. G., Serenelli A. M., Benvenuto O. G., 2001, *MNRAS*, 323, 471
- Anders E., Grevesse N., 1989, *Geochimica et Cosmochimica Acta*, 53, 197
- Asplund M., Gustafsson B., Lambert D. L., Rao N. K., 2000, *A&A*, 353, 287
- Benvenuto O. G., Althaus L. G., 1998, *MNRAS*, 293, 177
- Blöcker T., 1995, *A&A*, 297, 727
- Clayton G. C., 1996, *PASP*, 108, 225
- Clayton G. C., 2012, *Journal of the American Association of Variable Star Observers (JAAVSO)*, 40, 539
- Clayton G. C., Geballe T. R., Herwig F., Fryer C., Asplund M., 2007, *ApJ*, 662, 1220
- Clayton G. C., Sugerman B. E. K., Stanford S. A., Whitney B. A., Honor J., 2011, *ApJ*, 743, 44
- Dan M., Rosswog S., Brüggen M., Podsiadlowski P., 2014, *MNRAS*, 438, 14
- Dan M., Rosswog S., Guillochon J., Ramirez-Ruiz E., 2011, *ApJ*, 737, 89
- Eggleton P. P., Fitchett M. J., Tout C. A., 1989, *ApJ*, 347, 998
- Ferguson J. W., Alexander D. R., Allard F., Barman T., Bodnarik J. G., Hauschildt P. H., Heffner-Wong A., Tamanai A., 2005, *ApJ*, 623, 585
- Gautschi A., Glatzel W., 1990, *MNRAS*, 245, 597
- Grevesse N., Sauval A. J., 1998, *Space Science Reviews*, 85, 161
- Han Z., 1998, *MNRAS*, 296, 1019
- Heber U., 1983, *A&A*, 118, 39
- Hurley J. R., Pols O. R., Tout C. A., 2000, *MNRAS*, 315, 543
- Hurley J. R., Tout C. A., Pols O. R., 2002, *MNRAS*, 329, 897
- Iben I., Renzini A., 1984, *Physics Reports*, 105, 329
- Jeffery C. S., Hamann W.-R., 2010, *MNRAS*, 404, 1698
- Jeffery C. S., Karakas A. I., Saio H., 2011, *MNRAS*, 414, 3599
- Jeffery C. S., Saio H., 1999, *MNRAS*, 308, 221
- Jeffery C. S., Saio H., 2013, *MNRAS*, 435, 885
- Lambert D. L., 1986, in K. Hunger, D. Schoenberner, & N. Kameswara Rao ed., *IAU Colloq. 87: Hydrogen Deficient Stars and Related Objects Vol. 128 of Astrophysics and Space Science Library*, The chemical composition of cool stars. II - The hydrogen deficient stars. pp 127–147
- Landau L., Lifshitz E., 1962, in *The classical theory of fields*. Pergamon, Oxford., . pp 1–352
- Lau H. H. B., Stancliffe R. J., Tout C. A., 2008, *MNRAS*, 385, 301
- Livio M., Soker N., 1988, *ApJ*, 329, 764
- Longland R., Lorén-Aguilar P., José J., García-Berro E., Althaus L. G., 2012, *A&A*, 542, A117
- Longland R., Lorén-Aguilar P., José J., García-Berro E., Althaus L. G., Isern J., 2011, *ApJL*, 737, L34
- Lorén-Aguilar P., Isern J., García-Berro E., 2009, *A&A*, 500, 1193
- Lynden-Bell D., Pringle J. E., 1974, *MNRAS*, 168, 603
- Marsh T. R., Nelemans G., Steeghs D., 2004, *MNRAS*, 350, 113
- Menon A., Herwig F., Denissenkov P. A., Clayton G. C., Staff J., Pignatari M., Paxton B., 2013, *ApJ*, 772, 59
- Meyer B. S., 1994, *ARAA*, 32, 153
- Miller G. E., Scalo J. M., 1979, *ApJS*, 41, 513
- Motl P. M., Frank J., Tohline J. E., D’Souza M. C. R., 2007, *ApJ*, 670, 1314
- Nelemans G., Portegies Zwart S. F., Verbunt F., Yungelson L. R., 2001, *A&A*, 368, 939
- Pandey G., Lambert D. L., Jeffery C. S., Rao N. K., 2006, *ApJ*, 638, 454
- Pandey G., Lambert D. L., Rao N. K., 2008, *ApJ*, 674, 1068
- Paxton B., Bildsten L., Dotter A., Herwig F., Lesaffre P., Timmes F., 2011, *ApJS*, 192, 3
- Raiteri C. M., Busso M., Picchio G., Gallino R., Pulone L., 1991, *ApJ*, 367, 228
- Raskin C., Scannapieco E., Fryer C., Rockefeller G., Timmes F. X., 2012, *ApJ*, 746, 62
- Saio H., 2008, in Werner A., Rauch T., eds, *Hydrogen-Deficient Stars Vol. 391 of Astronomical Society of the Pacific Conference Series*, Radial and Nonradial Pulsations in RCB and EHe-B Stars. p. 69
- Saio H., Baker N. H., Gautschi A., 1998, *MNRAS*, 294, 622
- Saio H., Jeffery C. S., 2002, *MNRAS*, 333, 121
- Staff J. E., Menon A., Herwig F., Even W., Fryer C. L., Motl P. M., Geballe T., Pignatari M., Clayton G. C., Tohline J. E., 2012, *ApJ*, 757, 76
- Steinfadt J. D. R., Bildsten L., Arras P., 2010, *ApJ*, 718, 441
- Tang S., Cao Y., Bildsten L., Nugent P., Bellm E., Kulkarni

- S. R., Laher R., Levitan D., Masci F., Ofek E. O., Prince T. A., Sesar B., Surace J., 2013, *ApJL*, 767, L23
- Tisserand P., Marquette J. B., Wood P. R., Lesquoy É., Beaulieu J. P., et al. 2008, *A&A*, 481, 673
- van den Heuvel E. P. J., 1976, in Eggleton P., Mitton S., Whelan J., eds, *Structure and Evolution of Close Binary Systems Vol. 73 of IAU Symposium, Late Stages of Close Binary Systems*. p. 35
- Ventura P., D’Antona F., Mazzitelli I., 2000, *A&A*, 363, 605
- Ventura P., Di Criscienzo M., Carini R., D’Antona F., 2013, *MNRAS*, 431, 3642
- Wang B., Meng X., Chen X., Han Z., 2009, *MNRAS*, 395, 847
- Warner B., 1967, *MNRAS*, 137, 119
- Webbink R. F., 1984, *ApJ*, 277, 355
- Whittet D. C. B., ed. 2003, *Dust in the galactic environment*
- Wood P. R., 1976, *MNRAS*, 174, 531
- Yoon S., Podsiadlowski P., Rosswog S., 2007, *MNRAS*, 380, 933
- Zaniewski A., Clayton G. C., Welch D. L., Gordon K. D., Minniti D., Cook K. H., 2005, *AJ*, 130, 2293
- Zhang X., Jeffery C. S., 2012a, *MNRAS*, 426, L81
- Zhang X., Jeffery C. S., 2012b, *MNRAS*, 419, 452
- Zhu C., Chang P., van Kerkwijk M. H., Wadsley J., 2013, *ApJ*, 767, 164